Atomic-resolution imaging of oxidation states in manganites

M. Varela,[1] M. P. Oxley,[2,1] W. Luo,[2,1] J. Tao,[1,*] M. Watanabe,[3,†] A. R. Lupini,[1] S. T. Pantelides,[2,1] and S. J. Pennycook[1,2]
[1]*Oak Ridge National Laboratory, Oak Ridge, Tennessee 37831, USA*
[2]*Vanderbilt University, Nashville, Tennessee 37235, USA*
[3]*National Center for Electron Microscopy, Lawrence Berkeley National Laboratory, Berkeley, California 94720, USA*
(Received 23 July 2008; revised manuscript received 21 January 2009; published 23 February 2009)

Aberration corrected electron optics allows routine acquisition of high spatial resolution spectroscopic images in the scanning transmission electron microscope, which is important when trying to understand the physics of transition-metal oxides such as manganites. The physical properties of these perovskites are intimately related to the occupancies of the partially filled 3*d* bands, which define their oxidation state. In this work, we review procedures to obtain this electronic property in $La_xCa_{1-x}MnO_3$ from atomic-column-resolved electron energy-loss spectra measured in the aberration corrected scanning transmission electron microscope. In bulk samples, several features of both the average Mn $L_{2,3}$ edge and the O *K* edge fine structure change linearly with Mn nominal valence. These linear correlations are extracted and used as a calibration to quantify oxidation states from atomic resolution spectroscopic images. In such images, the same fine-structure features exhibit further changes, commensurate with the underlying atomic lattice. Mn valence values calculated from those images show unexpected oscillations. The combination of experiment with density-functional theory and dynamical scattering simulations allows detailed interpretation of these maps, distinguishing dynamical scattering effects from actual changes in electronic properties related to the local atomic structure. Specifically, in $LaMnO_3$, the two nonequivalent O sites can be distinguished by these methods.

DOI: 10.1103/PhysRevB.79.085117 PACS number(s): 75.47.Lx, 79.20.Uv, 68.37.Ma

I. INTRODUCTION

Transition metal oxides (TMO) with perovskite or related structures exhibit a rich variety of physical properties such as high T_c superconductivity, ferroelectricity, or colossal magnetoresistance, many of which are still not fully understood. Further understanding of this plethora of behaviors relies on experiments capable of simultaneously mapping structural, chemical, and especially, electronic features with adequate spatial resolution. This capability is of the utmost importance since some of these macroscopic phenomena are intimately related to the presence of an electronic inhomogeneity of some sort at nanometric (or shorter) length scales (e.g., electronic phase separation, striping, etc.).[1] TMO electronic properties are intimately related to the partially filled 3*d* shells of the transition-metal atoms, which are strongly hybridized with the O 2*p* bands. The resulting density of states (DOS) around the Fermi level can be probed by several spectroscopic techniques. Electron energy-loss spectroscopy (EELS) in the scanning transmission electron microscope (STEM) is capable of providing measurements of atomic positions and electronic properties in real space with atomic resolution.[2–5] In recent years, aberration correctors have been successfully implemented in the STEM, and postspecimen electron optics has been vastly improved. Finally, direct simultaneous probing of the structure, chemistry, and electronic properties of materials with atomic resolution and single atom sensitivity is routinely attainable.[3,6–9]

In this context, the possibilities for exploring oxide materials using atomic resolution EELS imaging become truly exciting. EELS techniques are ideally suited for chemical imaging purposes since the intensity under any absorption edge depends on elemental concentration.[10] In addition, electron energy loss near-edge structures (NES) can be used to measure magnitudes related to the atomic bonding such as the transition-metal oxidation states.[11–14] This work's main focus is to study these relations in the well-known $La_xCa_{1-x}MnO_3$ (LCMO) system. $LaMnO_3$ (LMO) is an antiferromagnetic insulator that becomes ferromagnetic upon doping of holes in the Mn 3*d* e_g band. This can be achieved by doping LMO with Ca, introducing such holes and generating a mixed-valence system which is responsible for the colossal magnetoresistance found in these materials.[1] We will show how changes in the near-edge fine structures of both the Mn $L_{2,3}$ (around 640 eV) and the O *K* edges (around 530 eV) are observed when the oxidation state is modified this way. Then we will investigate further changes taking place in EELS images obtained at atomic resolution. We will show how extracting information from such atomic resolution EELS images is not a straightforward task. For proper interpretation, both dynamical simulations of electron-beam propagation and density-functional theory calculations of the density of states in the presence of the core hole will be needed since the spectral features of interest depend on the relative position of the electron beam and the atomic columns. Specifically we will compare three different methods to extract oxidation states, the normalized O *K* pre-peak intensity, the energy separation between the pre-peak and main peak, and the ratio of the L_3 to L_2 white lines. These features originate from different interactions with the fast electron, involve different matrix elements, different final states, and therefore may be expected to show different variations across the unit cell as the probe is scanned. Our aim in this paper is to identify the proper conditions to extract oxidation states with atomic resolution. Furthermore, it will be shown how to spectroscopically identify nonequivalent O atoms in the material, opening new avenues toward real-space studies of the relationship between minor structural and orbital distortions in the material's electronic properties.

II. METHODS

STEM and EELS are combined here with first-principles calculations. Most of the STEM-EELS measurements here have been acquired using a VG Microscopes HB501UX operated at 100 kV and equipped with an Enfina EEL spectrometer and a Nion aberration corrector. LCMO samples synthesized by different methods have been used in this study. LMO and $CaMnO_3$ (CMO) powders were synthesized by conventional solid sate reaction methods. Powder samples were crushed and dispersed on a holey C film to produce suitable STEM specimens. A $La_{0.7}Ca_{0.3}MnO_3$ thin film around 100 nm thick was grown by high oxygen pressure sputtering and prepared in plan view geometry by conventional thinning, dimpling, and Ar ion milling including a final low-voltage cleaning. $La_{0.55}Ca_{0.45}MnO_3$ and $La_{0.33}Ca_{0.67}MnO_3$ powders were sintered into a pellet and the resulting polycrystalline samples were thinned, and ion milled to produce thin specimens suitable for TEM. The $x=0.33$ material was studied in a JEOL 2010F microscope. All the samples were tilted to a pseudocubic zone axis for STEM-EELS observations, which were performed at room temperature. EEL spectra were typically acquired from relatively thin regions, with thickness values in terms of the inelastic mean-free path $t/\lambda < 0.5$.

EELS O *K* edge simulations for LMO and CMO were performed using the $Z+1$ approximation as described in Ref. 15 and 55. Image simulations based on core-loss EELS were performed with dynamical scattering included using a frozen phonon code.[16–18] The calculations used a detector semiangle of 12 mrad and an energy window of 40 eV above threshold. A 28 mrad probe forming aperture was used and balanced aberrations typical of the HB501UX assumed with defocus, third and fifth order spherical aberrations being $\Delta f = 62$ mm, $C_s = -0.05$ mm, and $C_5 = 63$ mm, respectively.

III. AVERAGED QUANTIFICATION OF THE Mn OXIDATION STATE THROUGH THE Mn $L_{2,3}$ EDGE

Transition metal *L* edges result from excitations of $2p$ electrons into empty bound states or the continuum. Thus, these edges show two characteristic features or white lines originating from transitions from the spin orbit split $2p_{3/2}$ and $2p_{1/2}$ levels to the available states in the $3d$ band (generally, for the small scattering angles involved in EELS experiments the dipole approximation holds). The intensity ratio between these lines (L_3/L_2, also known as L_{23} intensity ratio or simply L_{23} ratio) should be two, on the basis of the $2j+1$ degeneracy of the initial core state in a one-electron model. However, L_{23} ratios are often very different from this expected value.[19,20] It has been proposed that such deviations arise from interactions between the $3d$ electrons, the core hole and the excited electron,[21,22] or from Coulomb and exchange interactions between *p* and *d* electrons.[23] So far, theoretical simulations of transition metal $L_{2,3}$ edges have been successfully achieved in metals,[24] but for oxides only multiplet based calculations[25–27] have been able to fully reproduce actual L_{23} values across the full range of oxidation states. Experimentally, the L_{23} ratio increases with the number of electrons in the $3d$ bands across the periodic table when going from the $3d^0$ toward $3d^5$ configuration (where a maximum is reached), and then decreases toward the $3d^{10}$ configuration.[21–23,28] In addition, for a given $3d$ metal such as Mn, the L_{23} ratio decreases when the Mn oxidation state (defined as seven minus the $3d$ band occupancy) increases from +2 to +7.[14,21,28]

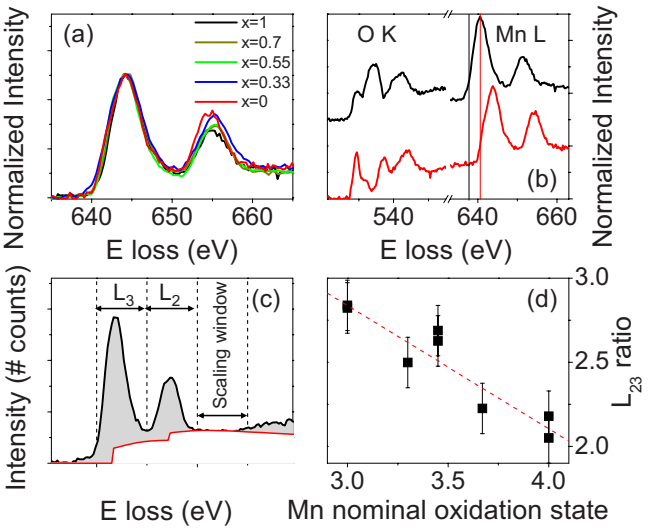

FIG. 1. (Color online) (a) Mn $L_{2,3}$ edges for a series of $La_xCa_{1-x}MnO_3$ compounds with $x=1$ (black), $x=0.7$ (dark yellow), $x=0.55$ (green), $x=0.33$ (blue), and $x=0$ (red). These spectra have been acquired from wide sample areas (by defocusing the electron beam or by averaging a number of spectra from different locations). The energy scale is nominal, and has been shifted and the intensity normalized so the L_3 lines match. (b) EEL spectra showing the O *K* edge around 530 eV and the Mn *L* edge around 640 eV for LMO (black) and CMO (red). The spectra have been displaced vertically for clarity. (c) Sketch showing a generic Mn $L_{2,3}$ edge (black line) and the approximate position of the windows used for integration of the L_3 and L_2 line intensities, and also the window used to scale the Hartree-Slater cross-section step function (red line). After scaling and subtraction of this function, the remaining signals under the L_3 and L_2 lines (shaded) are integrated, and their ratio is calculated. (d) Dependence of the L_{23} ratio with the formal oxidation state for a series of LCMO compounds. The red dashed line represents a linear fit to the data.

For Mn, the L_3 line can be found around 644 eV and the L_2 around 655 eV. Figure 1(a) shows a series of Mn $L_{2,3}$ spectra from a set of $La_xCa_{1-x}MnO_3$ samples with $x=1$, 0.7, 0.55, 0.33, and 0. Ca doping progressively increases the hole doping of the Mn $3d$ e_g band, so the electronic configuration of this sample set evolves from the $t_{2g}^3e_g^1$ configuration of LMO to the $t_{2g}^3e_g^0$ of CMO. The general view is that the Mn subsystem is in a mixed-valence state consisting of a mixture of Mn^{+3} and Mn^{+4}, with the Mn^{+3}/Mn^{+4} ratio equal to $x/(1-x)$. Thus, the nominal oxidation states for the materials in Fig. 1(a) are +3, +3.3, +3.45, +3.67, and +4, respectively. Clearly, the relative intensity of the L_2 line with respect to the L_3 line in Fig. 1(a) increases as the nominal oxidation state of Mn increases from +3 (for LMO, black curve) to +4 (CMO, red curve). This effect can be quantified and a phenomenological relationship between the L_{23} intensity ratio and Mn oxidation state will be described later. To allow the

direct visual comparison of the data, the spectra intensities in Fig. 1(a) have been normalized to the L_3 line intensity and an energy shift of a few eV applied so that the L_3 edges are aligned.

Chemical shifts also occur upon variation of the 3*d* metal oxidation state.[12,13] Absolute values of energy thresholds are difficult to obtain experimentally, so all the energy scales through this work are approximate. Under the assumption that the O *K* edge is invariant, a measure of the Mn $L_{2,3}$ edge chemical shift can be made by comparing its position relative to the O *K* edge onset. Such measurement only depends on the stability of the energy dispersion. Figure 1(b) shows the O *K* and Mn $L_{2,3}$ edges for the parent compounds LMO (top) and CMO (bottom), aligned at the O *K* onset. A clear shift of a few eV (below 3 eV) between Mn $L_{2,3}$ edge onsets (marked with vertical lines) is observed as expected.[8,12,13] This shift is in good agreement with previous reports, but given the experimental difficulty of calibrating the energy scales we will not use chemical shifts to study electronic properties here.

Fortunately, analyzing the L_{23} intensity ratio allows the extraction of reliable electronic information, independent of the absolute energy scale. Such analysis is a complex process, since *L* white lines are superimposed on less intense transitions to continuum states.[10] The intensity contributed by the continuum needs to be removed before extracting the L_{23} intensity ratio (to which only transitions to bound states should contribute). Thickness effects may also play a role in the L_{23} ratio so we use relatively thin samples. Different methods have been used to quantify L_{23} intensity ratios in the literature.[11,14,20,21,28–31] Here, we will first remove the background below the Mn $L_{2,3}$ edge using a power-law fit and then remove the continuum contribution by scaling a step function and subtracting it from the Mn $L_{2,3}$ edge as illustrated in Fig. 1(c). As a step function we use a Hartree-Slater cross-section function as available in Digital Micrograph.[32,33] For scaling purposes, a 10 eV wide window placed right after the L_2 line is used. Next, the remaining signal under the corrected L_3 and L_2 lines is integrated within two 10 eV wide windows, the first one placed at the onset of the L_3 line, and the second one next to the first as shown in Fig. 1(c). The resulting integrated intensity values are then used to calculate the L_{23} intensity ratio. It is worth noting that error bars for such a method may sometimes be relatively large (up to 5%–10%). This can be the case if signal-to-noise ratios (SNR defined as the maximum edge intensity divided by the total noise per spectrum channel[22]) in the data are poor: noise can severely affect the step-function scaling process. Therefore it is important to work with EELS data with as little noise as possible. Slight changes in positioning of the integration windows can also affect the L_{23} quantification, but this effect is usually smaller.

L_{23} ratios extracted this way are plotted versus the Mn nominal oxidation state for a number of $La_xCa_{1-x}MnO_3$ samples in Fig. 1(d). As expected, the L_{23} value decreases with increasing oxidation state, in good agreement with previous reports.[14,28–31,34] In particular, L_{23} values measured here for the parent compounds LMO and CMO are consistent with previous values reported in the literature for Mn compounds with oxidation states of +3 and +4, respectively.[14,28–31,34] Error bars were estimated by varying the position of the integration windows and comparing the resulting L_{23} ratios. Within such error bars, the data points in Fig. 1(d) seem to follow a linear trend, allowing a linear fit (red dashed line) to the data. The fitting parameter values obtained for a linear regression (least-squares method using Origin) $y=a+bx$ are $a=5.0\pm0.4$ and $b=-0.73\pm011$. The fitting correlation coefficient value is $r=0.933$. This fit will be used in what follows as a calibration to obtain Mn oxidation states from L_{23} ratio values. It is worth noting that we also used other methods reported in the literature to estimate the L_{23} ratio from our data.[19,22,31] The results obtained agree reasonably well with the analysis presented here, except for one of the methods described by Riedl *et al.* in Ref. 22 where L_{23} ratios are calculated with no continuum correction, which we found to be too dependent on sample thickness.

IV. QUANTIFICATION OF THE Mn OXIDATION STATE FROM THE ANALYSIS OF THE O *K* EDGE FINE STRUCTURE

In the dipole approximation, the O *K* edge (around 530 eV) provides information on excitations of O 1*s* electrons to the 2*p* bands. The O *K* near-edge fine structure also shows significant changes when the Mn oxidation state is modified. Three main features are found in the near-edge fine structure (see Fig. 2): a pre-peak right at the onset, around 530 eV, a second peak around 535 eV, attributed to hybridization with La 5*d* and/or Ca 3*d* bands, and a third peak around 540 eV where mainly Mn 4*sp* type bands contribute. The pre-peak has a strong Mn 3*d* band contribution and is extremely sensitive to bonding features.[14] Since the t_{2g} band of LCMO is fully occupied, this feature has a very strong contribution from the Mn 3*d* e_g band.[23,35–38] Hence, pre-peak analysis will allow information on the Mn 3*d* band occupancy (i.e., oxidation state or valence) to be extracted.

Figure 2(a) shows a set of O *K* edges from a number of LCMO samples with increasing values of Ca doping, $(1-x)$. Spectra have been displaced vertically for clarity. As expected from simple band occupation arguments, the pre-peak feature is largely diminished in the LMO compound, while it is fully developed in the CMO spectrum. For compounds with intermediate compositions the pre-peak intensity increases monotonically relative to that of the second peak. A robust method of quantifying the pre-peak intensity is illustrated in Fig. 2(b). To quantify this variation, Gaussians are fitted to both the pre-peak (red line) and the main peak (blue line). The normalized pre-peak intensity is then defined as the ratio of the areas under the red and blue Gaussians curves, respectively. In this way, extrinsic effects such as those related to sample thickness or O concentration are removed. When this normalized pre-peak intensity is plotted against the Mn nominal oxidation state for our series of LCMO materials a linear behavior is found, as shown in Fig. 2(c). The dashed red line in Fig. 2(c) is a linear fit to the data points and can be used as a calibration curve to extract the Mn valence from future measurements of pre-peak normalized intensities. For this $y=a+bx$ fit, the parameter values found are $a=-0.49\pm0.11$ and $b=0.25\pm0.03$. The *r* coefficient value provided by the Origin linear fit routine is $r=0.959$.

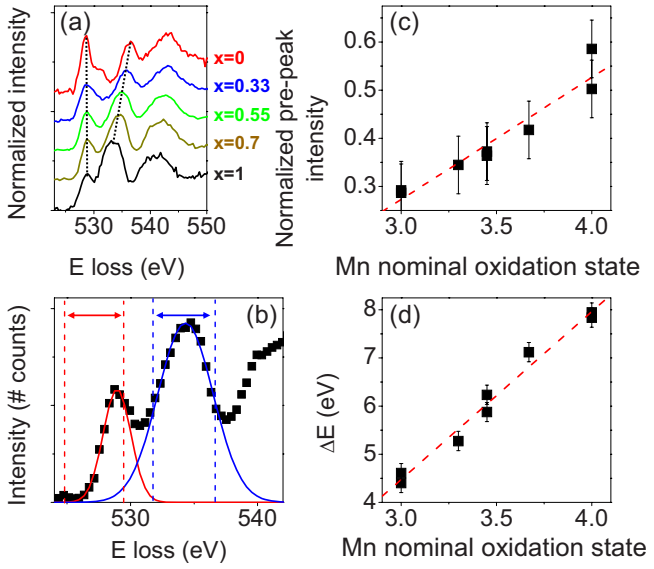

FIG. 2. (Color online) (a) Spatially averaged O *K* edges for a series of LCMO compounds with $x=1$ (black), $x=0.7$ (dark yellow), $x=0.55$ (green), $x=0.33$ (blue), and $x=0$ (red). The energy scale has been shifted so the pre-peaks are aligned, and the intensity normalized. A minor splitting of the CMO pre-peak is observed. Vertical dotted lines show the positions of the pre-peak and the adjacent main peak. The spectra have been displaced vertically for clarity. (b) O *K* EEL spectrum showing the Gaussian curves used to extract peak intensity and position (pre-peak in red and main peak in blue). In both cases a window 5 eV wide (approximately) was used for the fitting, their approximate positions marked with vertical dashed lines. The pre-peak fitting window was displaced to the left so that just a few channels at the peak maximum were included. This way, the split pre-peak feature observed in CMO was avoided. Again, the error bars have been estimated by shifting laterally a few pixels the Gaussian fitting windows. Since the second peak is very well defined, this procedure has a small effect on its fit. (c) Normalized pre-peak intensity versus nominal oxidation state for the series of LCMO samples. The red dashed line is a linear fit to the data, with a regression coefficient of $r=0.959$. (d) Energy separation (calculated as the difference between positions of the second peak and the pre-peak) as a function of the Mn nominal oxidation state for the sample set of samples. Again, the red dashed line represents a linear fit to the data (in this case, $r=0.990$).

Interestingly, there is a second, independent, feature in the O *K* edge fine structure that correlates with Mn valence. The difference in peak positions between the pre-peak and the adjacent main peak, ΔE, increases steadily with Ca doping [marked with black dotted lines in Fig. 2(a)]. The same Gaussian fits used to extract pre-peak intensities in Fig. 2(b) allow the accurate quantification of peak positions. Figure 2(d) shows the dependence of ΔE on the nominal Mn oxidation state for our LCMO series, and reveals a very clear linear correlation. This dependence has been previously hinted at Refs. 11, 13, and 22, and was attributed to a chemical-potential shift of the initial core and the final states of the ejected electron.[22] It is worth noting that since the peak positions are less dependent on noise than peak areas extracted from the Gaussian fits, the error bars associated with ΔE are noticeably smaller than those of the pre-peak normalized intensity. Interestingly, a linear fit to the data [dashed red line on Fig. 2(d)] has a better fit coefficient of $r=0.990$ and smaller error bars, so it constitutes an excellent calibration curve for future reference. The linear regression parameter values in this case are $a=-6.0\pm0.7$ and $b=3.5\pm0.2$. Among the three methods examined so far to quantify Mn oxidation states, measurement of ΔE in these compounds is the most accurate.

V. EFFECT OF SAMPLE THICKNESS

An important factor to consider is the consistency of the extracted oxidation state to changes in specimen thickness. Figure 3 shows the results of the three analyses on an EELS line scan obtained from a CMO particle when moving the electron beam from the edge into relatively thick areas ($t/\lambda>1$). Sample thickness and ΔE, normalized pre-peak intensity and L_{23} ratio values are plotted. All parameters are basically independent of thickness except for a small increase in the L_{23} ratio in the thickest regions. Near the particle edge a slight decrease of ΔE and normalized pre-peak intensity is observed, while the L_{23} ratio increases. This is not due to a dependence on thickness but to a small oxygen deficiency near the particle edge, as observed in Fig. 3(f). This panel shows the Mn/O ratio calculated from the O *K* and the Mn $L_{2,3}$ edges as explained in the caption, using the Digital Micrograph routine. While in the bulk this ratio is close to 0.33, the nominal value expected, near the edge the Mn/O ratio increases up to almost 0.38. This increase denotes a slight oxygen deficiency, which causes the reduction in Mn suggested by the changes in the parameters above. It is worth noting that we did not observe this slight deoxygenation near the edges of LMO particles, where flat Mn/O ratio profiles consistent with a 1/3 ratio are found all the way to the edge of the crystals. In summary, we can conclude that our methods are independent of sample thickness within the range that we use in this work ($t/\lambda<0.5$).

VI. TOWARD ATOMIC RESOLUTION SPECTROSCOPIC IMAGES: NOISE REDUCTION TOOLS

Having established these calibrations, our thrust is to quantify Mn oxidation states from atomic resolution EELS spectrum images.[39,40] Atomic-resolution spectroscopic imaging of manganite bulk samples and films has been reported in very recent years,[4,5,9,41] but interpretation of such images is not a trivial task. The effective nonlocality of the underlying inelastic-scattering potential, and dynamical effects (electron channeling) have an important effect in the EELS image contrast.[16,17,42,43] Highly nonintuitive effects such as volcanolike features on atomic columns are often observed. These effects can be in part quantified and understood through multislice or frozen phonon calculations. But these calculations do not include solid-state effects, which give rise to the fine-structure detail of interest here. For a full interpretation of atomic resolution EELS images, complementary theoretical studies of the density of states through density-functional calculations are needed too. These are not trivial either since EELS measures the available density of states above the

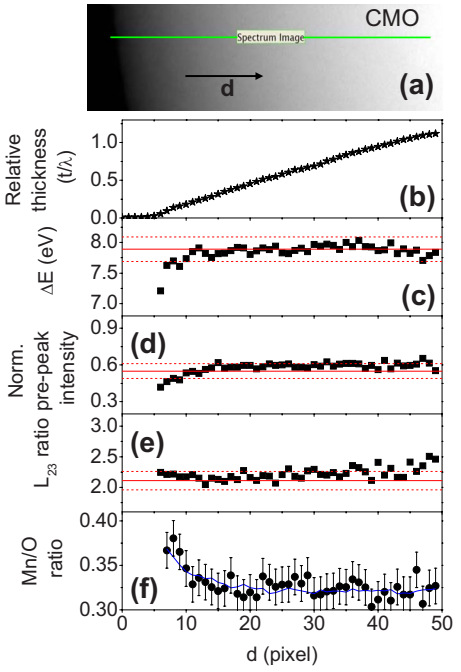

FIG. 3. (Color online) Effect of thickness on parameter quantification: (a) Annular dark field (ADF) image of a CMO particle. The region marked with a green line was used for acquisition of two line scans, one including the zero loss peak (acquisition time of 0.06 s per pixel) and another one for the core-loss region (using 10 s per pixel). The electron beam was defocused 20 nm to simulate average illumination. (b) Relative thickness along the line scan path in inelastic mean-free path units. (c) ΔE, (d) normalized pre-peak intensity, and (e) the L_{23} ratio along the scan. Horizontal solid red lines show the values of the average parameters for CMO reported in Figs. 1 and 2. Horizontal red dotted lines show the error bar amplitude as reported in Figs. 1 and 2. (f) Mn/O ratio, after subtracting the background using a power-law fit, and integrating the intensity remaining under the O K and the Mn $L_{2,3}$ edges. Integration windows of 35 and 40 eV were used, respectively. For the O K edge a Hartree-Slater cross section was employed, while for the Mn $L_{2,3}$ edge a hydrogenic (white line) cross section was used. When Hartree-Slater cross sections are employed for both edges a similar behavior is found in the data, with values shifted upward around 0.02 Mn/O ratio units (consistent with our error bars). The blue line is the same ratio after treating the EELS data with principal component analysis. Some oxygen deficiency is found near the edge. In fact, extended electron-beam irradiation in some of these ultrathin areas gives rise to the appearance of superstructures in the ADF images, which are typically assigned to ordering of O vacancies (Ref. 53).

Fermi level in the presence of the core hole left behind, which can be significantly different from the unperturbed density of states.[15,44–46]

Unfortunately, these studies are hampered by noise in the experimental EELS data, one of the most important problems to be faced. In order to minimize spatial drift and damage effects, EELS imaging experiments require the shortest possible acquisition times per spectrum. But this approach typically produces data where the SNR is poor. A straightforward way to obtain spectra with reduced noise level is to average individual spectra obtained from equivalent atomic positions along the line scan or spectrum image. This is a very effective approach to generate an average spectrum corresponding to a given atomic site. In the results described below we will obtain and compare average spectra from different atomic positions in order to establish quantitative trends in the data set. We will demonstrate how the averaged spectra with the beam on column vs off column show changes that are greater than the error bars. The next step is to attempt to investigate how these changes evolve spatially along the line scan or the two-dimensional (2D) image. Such an attempt may shed some light on the nature of any variations of electronic properties. Hence the need for more sophisticated noise reduction tools that may allow extraction of significant information on a spectrum-by-spectrum basis.

Principal component analysis (PCA, a multivariate statistical analysis method) is most helpful in order to reduce random noise from spectroscopic images. The rationale is to reduce the dimensionality of a large data set by finding the minimum number of variables that describes the original data without losing significant information. The implicit assumption in applying PCA to spectral data is that the important spectral features in the signal are strongly correlated and, in turn, that such correlation is significant because random noise would tend to be uncorrelated. By selecting only the strongest components PCA will therefore reduce noise, although it may not eliminate correlated noise or other artifacts that might be present in data recorded on a charge coupled device (CCD).[47,48] Therefore, we recover a better estimate for the signal subject to the assumptions listed above. If this is done with care, the assumptions made on the data are examined and other noise reduction methods are employed as a cross check, PCA can successfully eliminate those uncorrelated noise components that might mask relevant data features and hinder further analysis.[49] In our case, the EELS data have significant random noise which is effectively removed by PCA. Also, since our experiment is performed on a crystalline, periodic material, we might expect to find a result that shows the periodicity of the lattice. *A priori* knowledge on the magnitude of the signal variations across the cell will be confirmed from measurements on averaged raw spectra. Under these conditions, it is fair to state that through PCA the SNR can be substantially enhanced without loss of significant information.

A Scree plot, which is the logarithm of the eigenvalue plotted against the index of component, is a useful guide toward selecting the correct number of components when reconstructing the data set. Such a plot is shown in Fig. 4 for a LMO EELS image. Since the eigenvalues of random noise components decrease exponentially, they will form a straight line in a Scree plot. Thus, components that carry significant information (the principal components) can be distinguished from those associated with uncorrelated noise by the abrupt change in slope shown in Fig. 4. The processed signal is obtained by ignoring the components that behave like noise when reconstructing the image by resumming only the significant components weighted by their respective eigenvalues (which are a quantitative measure of their importance). Care must be taken when choosing the cutoff component since small changes in the spectrum may be present near the cutoff, as opposed to general features that will be described

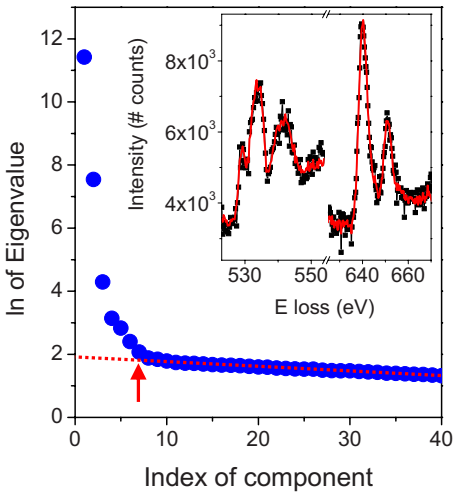

FIG. 4. (Color online) Scree plot after PCA has been performed on the EELS line scan in Fig. 7. A dotted red line highlights the portion of the plot where a flat behavior is observed (characteristic of uncorrelated noise). The red arrow points to the component index ($n=7$) where the deviation from this flat behavior is observed. Inset: raw EEL spectrum showing an O K edge and a Mn $L_{2,3}$ edge, extracted from Fig. 7(b) (black dots). The red line is the same spectrum after PCA.

by large eigenvalues. According to Fig. 4, seven components should be used for reconstruction of this particular data set. The inset shows some of the features of a typical spectrum extracted from a LMO EELS image: the O K edge and the Mn $L_{2,3}$ edge. The reconstructed EELS data (red line) are in excellent agreement with the as-obtained spectra (black dots) with no significant loss in spectral resolution, which would occur with Fourier filtering or averaging adjacent channels. All the relevant features and their intensities are properly reproduced after PCA. Further details of this data set will be presented in Fig. 7.

VII. ATOMIC RESOLUTION SPECTRUM IMAGES

These methods can easily be applied to one-dimensional (1D) EELS line scans and to two-dimensional EELS spectrum images in order to extract relevant information on electronic properties. In principle, 2D spectrum images may often be more convenient since they allow the probing of larger sample areas in a single experiment, hence showing better statistics and allowing noise reduction by rebinning if needed. Also, the effects of spatial drift (if present) can be easily identified and avoided during further analysis. Figure 5(a) shows a Z-contrast image of a CMO sample, again from a very thin region near the CMO particle edge (thickness estimated around 2–3 nm). A green rectangle marks the approximate area where the 2D EELS spectrum image was acquired. The CMO pseudocubic unit cell has been marked for clarity: a green circle for the Ca column and blue-yellow circles for Mn-O columns. Yellow crosses show the O columns in between. Figure 5(b) shows the simultaneously acquired annular dark field (ADF) signal (Z contrast), clearly showing the CMO crystal lattice (Mn-O columns appear

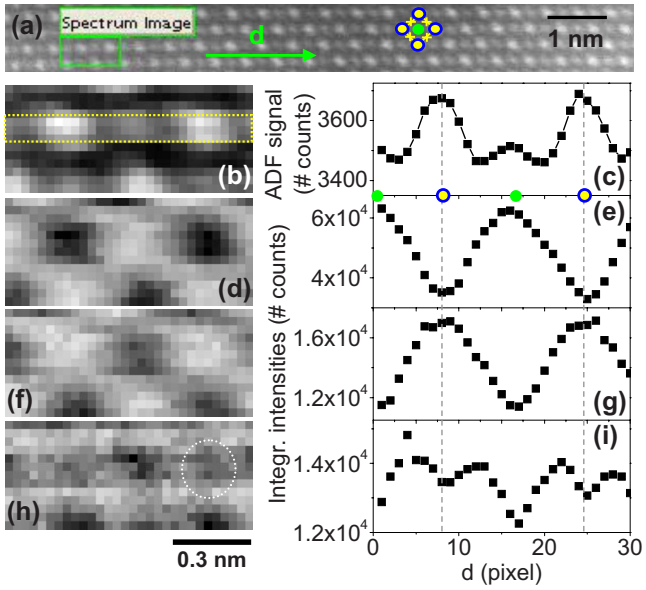

FIG. 5. (Color online) (a) Z-contrast image of a CMO sample tilted down the pseudocubic ⟨100⟩ zone axis. The cubic unit cell has been marked. A green rectangle highlights the approximate window for spectrum image acquisition. (b) ADF signal acquired simultaneously with the spectrum image in (a). (c) Averaged profile along the region marked with a yellow rectangle in (b). [(d), (f), and (h)] Ca $L_{2,3}$, Mn $L_{2,3}$, and O K images, respectively. [(e), (g), and (i)] Averaged profiles of (d), (f), and (h), respectively, using a window equivalent to the one depicted in (b). A white dotted circle shows the position of the volcano rim in (h). All EELS images have been generated by integrating a 35 eV wide window after background subtraction using a power-law fit from the EELS data after PCA. Green (blue-yellow) circles mark the approximate positions of Ca (Mn-O) columns along the scan.

bright, Ca columns dimmer). Spatial drift effects on this data set are observable, but minor. Figure 5(c) shows the ADF signal averaged over a window 4 pixels wide across the image [approximately, the area marked with yellow dotted rectangle in Fig. 5(b)]. For this image, an acquisition time of 0.7 s per pixel was used, and the data were processed with PCA. Figure 5(d) shows the 2D Ca $L_{2,3}$ image, while Fig. 5(e) shows the profile across a region equivalent to the one in Fig. 5(b). Figures 5(f) and 5(g) show the Mn $L_{2,3}$ image and its profile (averaged in the same way), while Figs. 5(h) and 5(i) show the equivalent O K image and corresponding profile. All of the elemental 2D images clearly show the individual chemical element lattice, well above noise levels. On top of that, Figs. 5(h) and 5(i) show the volcano structure expected for the O K image [a volcano rim is highlighted with a circle in Fig. 5(h)].[41] While both the Mn-O column and the surrounding O columns contain the same number of O atoms, the signal from the Mn-O column is reduced due to the electron probe being scattered beyond the EELS detector by the heavier Mn atoms. Similar features have been reported due to a difference in O concentration of adjacent columns,[4] but to the best of our knowledge these are the first experimental 2D images of such volcanoes due solely to different column composition ever reported. A smoothed version of Fig. 5(h), where the volcano geometry is more obvious to the eye, is shown in Fig. 6(a).

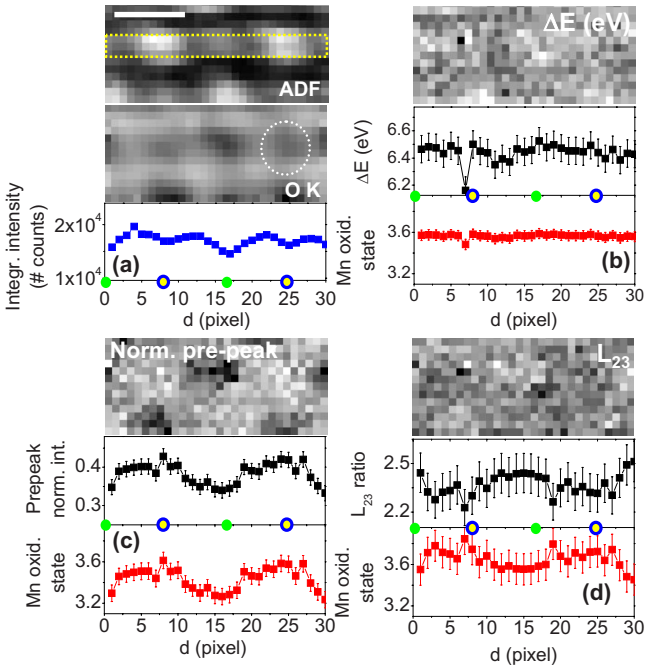

FIG. 6. (Color online) (a) The top panel ADF signal from Fig. 5(b). A yellow rectangle shows the area of the image used for averaging through the whole figure. The scale bar is approximately 0.3 nm. The middle panel shows a smoothed version of Fig. 5(h), where the volcano structure is more easily seen. A white dotted circle shows the position of the volcano rim. The lower panel is the O *K* integrated intensity from Fig. 5(i). (b) ΔE image (top), together with the averaged ΔE profile (black data points) and the derived Mn oxidation state (red). (c) Normalized pre-peak intensity image (top), together with the averaged profile (black data points) and the derived Mn oxidation state (red). (d) $L_{2,3}$ ratio image (top), with the averaged profile (black points) and the derived Mn oxidation state (red). Green (blue-yellow) circles mark the approximate position of Ca (Mn-O) columns along the scan in all cases, and all panels derive from PCA treated EELS data. The error bars through the averaged profiles are those of the original data, estimated from the errors of the Gaussian fits or from shifting the fitting, integration, or scaling windows a few pixels around and comparing the resulting values of the different parameters.

For the data in the spectrum image of Fig. 5, Fig. 6 shows the extracted 2D images of the different parameters described through this work and the derived Mn oxidation states. For averaging purposes a window marked with a dotted rectangle like the one in Figs. 5(b) and 6(a) was used in all cases. Figure 6(a) shows the ADF signal from Fig. 5(b) (top) and a smoothed O *K* image [derived from Fig. 5(h)], with its average profile. These facilitate the location of atomic-column positions through the rest of the figure. Blue-yellow (green) circles mark the approximate positions of the Mn-O (Ca) columns through the figure. Figure 6(b) shows the ΔE image (top), together with its average profile (black) and derived Mn oxidation state (red). Figure 6(c) shows an image of the normalized pre-peak integrated intensity (top), with its averaged profile (middle panel, in black) and the resulting Mn valence (red). Last, Fig. 6(d) shows the image of the L_{23} ratio (top), with its average profile (black) and the calculated Mn oxidation state (red). The average Mn oxidation states across the image obtained for the data in Fig. 6 are +3.43 ±0.11, +3.56 ±0.02, and +3.64 ±0.09 for the pre-peak intensity, the ΔE and the L_{23} ratio methods, respectively. Here the error bars are the standard deviation of the data set in the scan. The method that in principle seems more accurate, with less dispersion, is ΔE. The pre-peak method gives an average slightly low, and has the biggest error bars, so it seems the least reliable of the three. If we were, however, to use this method with the electron beam placed on the Mn-O column, the Mn oxidation state obtained would be near +3.56, identical to the average measured by ΔE. At this point we have no explanation for the different variation of these three methods across the unit cell. Regardless, all these images show a reduced Mn oxidation state near +3.5 or +3.6, instead of the expected +4 for CMO. We attribute this finding to the fact that this area of the sample, which is very thin (around 3 nm thick) and is close to the edge of the particle, is oxygen deficient. According to Fig. 3, for a similar thickness range the Mn/O ratio is approximately of 0.36, which roughly corresponds to 2.78 O atoms per Mn. This means that the local electron doping of 0.44 electrons per Mn, which amounts to an oxidation state of 3.56. This value is consistent with those found in Fig. 6.

While these images are rather noisy, even after PCA is applied to the data, an indication of atomic lattice contrast can be observed in some images. The L_{23} ratio image in Fig. 6(d) shows a slight dip at the Mn-O column positions, which produces a maximum Mn oxidation state on these columns when our bulk calibration is applied. The pre-peak image shows the most intense atomic contrast. These trends suggest that atomic resolution EEL spectra show behaviors in their features that differ from those of the average bulk spectra. In what follows we will focus our attention on studying these changes both in raw and PCA treated spectra. To do so, we have acquired 1D line scans instead of 2D images. 2D images typically require fairly short acquisition times per pixel in order to avoid severe spatial drift effects, and the extraction of reliable information on the NES may be complicated. Also, line scans allow the longest exposure times without a significant amount of damage since the electron beam only irradiates any given point of the sample once.

VIII. IMAGING OF OXIDATION STATES WITH ATOMIC RESOLUTION

Figure 7(a) shows a *Z*-contrast image of a LMO sample viewed down the pseudocubic ⟨100⟩ crystallographic axis. The maximum thickness of the sample was estimated to be around 13–15 nm from low loss images. This is an upper limit since no surface-plasmon contribution was taken into account.[10,50,51] The image shows the cubic structure of the manganite, with the brighter La columns, each surrounded by four dimmer Mn-O columns. A pseudocubic unit cell is marked. EELS images were acquired by moving the electron beam along the pseudocubic cell ⟨110⟩ diagonal while acquiring EEL spectra. Figure 7(b) shows one of these line scans, including the O *K* edge around 530 eV, the Mn $L_{2,3}$ edge around 640 eV and the La $M_{4,5}$ edge around 830 eV. The acquisition time per spectrum was 3 s, and the beam

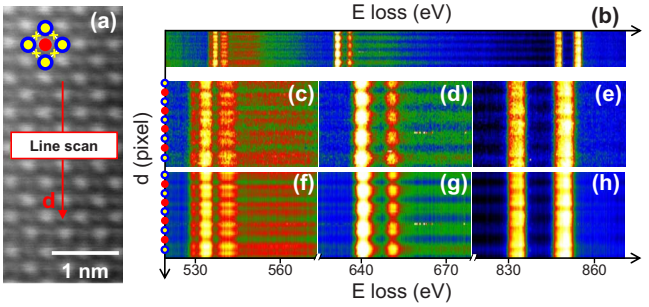

FIG. 7. (Color online) (a) *Z*-contrast image of a LMO sample viewed down the pseudocubic ⟨100⟩ zone axis. A pseudocubic unit cell is marked, with a red circle marking the La column position, and blue/yellow circles showing the Mn-O columns. Yellow crosses mark the approximate positions of pure O columns between Mn-O columns. (b) EELS line scan acquired along the direction of the red arrow in (a). [(c)–(e)] Magnified portions of (b), showing the O *K*, the Mn $L_{2,3}$ and the the La $M_{4,5}$ edges, respectively. [(f)–(h)] O *K*, Mn $L_{2,3}$, and La $M_{4,5}$ edge images in (c)–(e) after PCA, respectively. All of the EELS images show the rippling characteristic of atomic resolution EELS. The O *K* image shows a double ripple, characteristic of the volcano (as does the La $M_{4,5}$ image, although the contrast is not so strong). For figures (c)–(h) the approximate position of the La (Mn-O) columns is highlighted on the left with red (blue-yellow) circles.

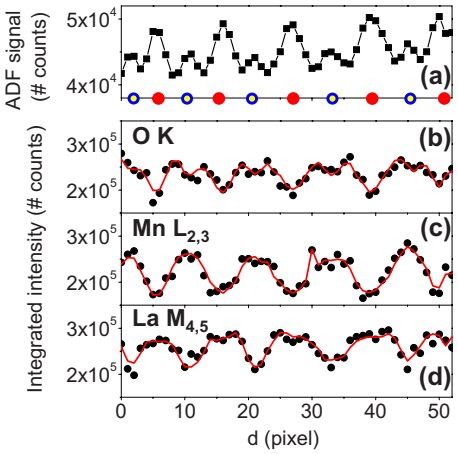

FIG. 8. (Color online) (a) ADF signal acquired simultaneously with the EELS line scan in Fig. 7. Red (blue-yellow) circles mark the approximate position of La (Mn-O) columns along the scan. La (Mn-O) columns show brighter (dimmer) on the ADF image. (b) O *K* image obtained by integrating the intensity under the O *K* edge after background subtraction. (c) Mn $L_{2,3}$ image. (c) La $M_{4,5}$ image. In all cases the black dots are the result of analyzing the raw EELS data, while the red line is the result after PCA analysis of the EEL spectra. A clear volcanolike structure is observed in the O *K* image (and just a hint of it in the La $M_{4,5}$ image)

current estimated to be of a few tens of picoamperes. The probe convergence semiangle was approximately 28 mrad. Figures 7(c)–7(e) show high magnification images of the regions around these three edges, respectively. PCA was applied to the EELS image (see the Scree plot for this line scan in Fig. 4). The resulting O *K*, Mn $L_{2,3}$ and La $M_{4,5}$ images are shown in Figs. 7(f)–7(h), respectively. For these images, the approximate positions of the La (Mn-O) columns are highlighted with red (blue and yellow) circles on the left side. The ripple observed in the EELS images reflects the atomic-column positions and shows that atomic resolution was achieved in the spectroscopic image. The spacing between these columns is not perfectly even due to minor sample drift during the image acquisition.

Figure 8(a) shows the ADF signal (*Z* contrast) acquired simultaneously with the line scan in Fig. 7. The integrated intensities for the O *K*, the Mn $L_{2,3}$ and the La $M_{4,5}$ edges are shown in Figs. 8(b)–8(d), respectively. For the EELS line scans, the black data points have been extracted by removing the background using a power law fitting and then integrating the intensity under the edge using a window of approximately 35 eV wide. The superimposed solid red line is the extracted intensity for the EELS images after being treated by means of PCA [i.e., extracted from Figs. 7(f)–7(h)], showing very good agreement with the analysis of the raw data. This is hardly unexpected since the integrated signal in effect minimizes random noise in any case. The minor disagreements observed are due to both the residual intensity and to the fact that the power-law fit to the background may vary slightly from the raw to the PCA treated data, even when the same fitting windows are used. These EELS images, together with the simultaneously acquired ADF signal, allow the atomic-column positions to be located. All the elemental line traces show a ripple that exhibits atomic periodicity. The Mn and O signals peak in the same position, as expected since these atoms lie in the same column. The La $M_{4,5}$ signal peaks in between Mn-O columns, as expected, and seems to show a somewhat flat volcanolike shape.[41] The O *K* edge image shows a volcanolike profile that will be discussed below. This volcano effect does not impede column location with EELS or chemical imaging with atomic resolution, although it can hinder the quantification of EELS measurements.

IX. INTERPRETATION OF ATOMIC RESOLUTION IMAGES

As noted above, the interpretation of images based on core-loss spectroscopy is complicated by issues such as the nonlocality of the effective ionization potential and the scattering of the incident electron probe through large angles by heavy atomic columns. The core-loss EELS signal can also be quite long ranged, meaning the EELS signal does not necessarily derive solely from the atomic column below the probe position. In Fig. 9(a) a schematic of the LMO/CMO manganite structure down the pseudocubic ⟨100⟩ projection is shown. We make the simplifying assumption that the perovskite structure is a perfect cube. The inclusion of distortions from this perfect structure does not strongly affect the dynamical channeling of the incident electrons and this approximation is a reasonable one in the qualitative discussion that follows. The contribution to the total O *K* signal in these images can thus be assumed to come from two distinct types of site, those columns containing O only, and those containing both Mn and O. Figures 9(b) and 9(c) show the contributions to the total O *K* signal from each of these sources for

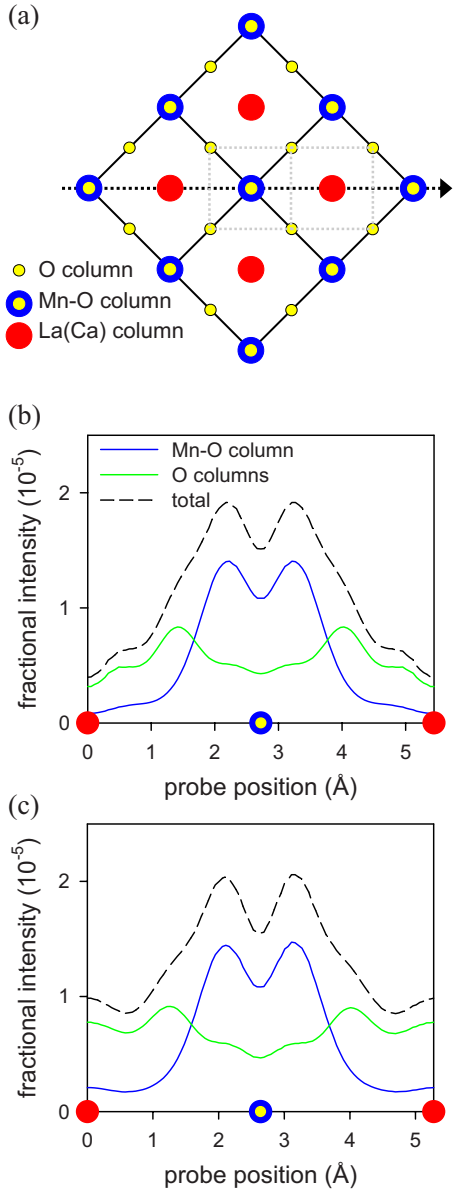

FIG. 9. (Color online) (a) Schematic of the manganite structure down the pseudocubic ⟨100⟩ projection. Red circles are the La (Ca) columns. Yellow circles are the O columns, and blue-yellow circles mark the Mn-O columns. The gray dotted squares indicate the nearest neighbors of a La (Ca) column and a Mn-O column, all of them pure O columns. An arrow points in the direction of the scan. (b) O *K* image frozen phonon simulations for a LMO sample 15 nm thick. The dashed line corresponds to the total O *K* signal. The blue line represents the contribution from the O atoms in the Mn-O columns, while the green line represents the contributions from the neighboring pure O columns. (c) O *K* image simulation for the CMO compound. Different line formats are coded as in (b).

LMO and CMO, respectively. Both simulations are done for a line scan along the ⟨110⟩ direction over alternating La(Ca) and Mn-O columns, as indicated by the dotted arrow in Fig. 9(a). Consider first the contribution to the signal from the O columns. Both the La(Ca) columns and Mn-O columns are surrounded by four nearest-neighbor O columns a little under 2 Å away. For the case of LMO, the O *K* signal above the

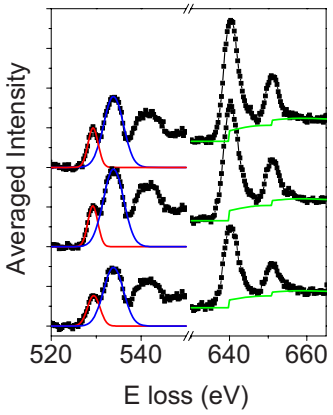

FIG. 10. (Color online) Averaged raw EEL spectra (black points) showing the O *K* edge and the Mn $L_{2,3}$ edge. Each spectrum is the result of averaging eight individual EEL spectra from three different positions along the scan in Fig. 7: La column (bottom), rim of the volcano of the Mn-O column (middle), and dip of the volcano on the Mn-O column (top). The red and blue curves show, for each case, the Gaussian fits for the pre-peak and the main peak, respectively. The green lines are the scaled Hartree-Slater step functions for L_{23} ratio quantification. The curves have been displaced vertically for clarity.

La column is smaller than that above the Mn-O column. This is due to the heavier La atoms leading to more high-angle scattering beyond the EELS detector. The converse is true for the CMO shown in Fig. 9(c), where the signal from the O columns above the Ca column is greater than that above the Mn-O column, again due to the increased high-angle scattering of Mn compared to Ca.

The relevant question now is whether information on electronic properties (such as the oxidation state, or the DOS) can be extracted from these images with atomic resolution. In order to study these effects we will perform an analysis of the spectral Mn $L_{2,3}$ and O *K* edges using the methods established in Figs. 1 and 2 (the described linear fits will be used as calibration curves). First, we will look for general trends on averaged raw EEL spectra, produced by averaging eight individual spectra extracted from equivalent positions along the line scan and then we will proceed to the analysis of the whole line scan looking at both the raw and the PCA treated signals.

Figure 10 shows three averaged EELS spectra from three positions along the scan in Fig. 8(b): from the volcano dip, the volcano rim, and the minimum in between (i.e., the La column). Each one is the result of averaging eight raw EEL spectra, which results in significant reduction in noise. The red and blue curves on the spectra show the results of fitting a Gaussian peak to the pre-peak and the main peak, respectively, as done in Fig. 2. The green curves are the scaled Hartree-Slater step functions, as described in Fig. 1. The resulting ΔE and normalized pre-peak intensities, and also the L_{23} intensity ratio from the Mn $L_{2,3}$ edge, are shown in Table I. Error bars are estimated again by shifting the fitting windows a few pixels and comparing results. Note that while some values have overlapping error bars the trends are quantitatively and qualitatively the same as observed in PCA treated data.

TABLE I. Parameters obtained from the analysis of the averaged raw EEL spectra from the La column position, and the Mn-O column (distinguishing between the volcano rim and the volcano dip positions).

	La column	Mn-O column (volcano rim)	Mn-O column (volcano dip)
ΔE (eV)	4.39 ± 0.07	4.59 ± 0.07	4.53 ± 0.07
Normalized pre-peak intensity	0.33 ± 0.02	0.26 ± 0.02	0.29 ± 0.02
L_{23} ratio	2.67 ± 0.01	2.65 ± 0.01	2.66 ± 0.01

Interestingly, both the parameters obtained from the fit of the O *K* edge show noticeable changes in these three different positions. The ΔE parameter is significantly lower on the La column, while it increases on the Mn-O columns. On the other hand, the normalized pre-peak intensity is maximum on the La column, and decreases on the Mn-O columns (showing a slight enhancement on the center of the column, in the volcano dip). The L_{23} ratio is the parameter that shows the least noticeable changes when shifting the electron beam to a different position. While a minor increase is observed on the La column, the change is too close to the error bar to draw a significant conclusion. However, it is worth noting that the L_{23} map shown in Fig. 6(d) also shows a slight increase in the L_{23} ratio on the Ca columns. The fact that the O *K* edge derived parameters (and perhaps to a lesser extent, the L_{23} ratio) show significant changes along the scan suggests that care must be taken when obtaining oxidation states in these compounds with atomic size electron probes. These changes are most puzzling, so in what follows we will examine these effects along the whole line scan.

Figure 11 shows the result of the same analysis for the complete LMO line scan along the ⟨110⟩ pseudocubic diagonal in Fig. 7 for the raw EEL spectra, and after PCA. The upper panel, Fig. 11(a), shows the O *K* integrated intensity (after PCA), which allows the Mn-O column positions to be located. For the rest of the figure, red lines denote analysis after PCA while black dots are the analysis of raw data. Figure 11(b) shows the behavior of the difference in energy, ΔE, between the pre-peak and the adjacent peak extracted from the O *K* edge along the line scan and the Mn oxidation state extracted from ΔE. Figure 11(c) represents the O *K* edge normalized pre-peak intensity together with the derived Mn valence. Figure 11(d) depicts the L_{23} ratio and the Mn oxidation state calculated from the L_{23} values. Error bars have been estimated again by shifting the fitting windows a few pixels and comparing the resulting values. Average values of Mn valence after PCA (raw) for all data sets are consistent with the nominal composition: values of 2.99 ± 0.03 (2.98 ± 0.07), 3.08 ± 0.07 (3.1 ± 0.2), and 3.00 ± 0.12 (3.0 ± 0.5) are found, respectively, for the ΔE, the pre-peak intensity and the L_{23} ratio methods. The error bars estimated for these averages are the standard deviation of every data set. These values are all in relatively good agreement with the nominal +3 expected. The data obtained from the L_{23} ratio have higher dispersion and show more noise, while the values obtained through ΔE analysis present lower disper-

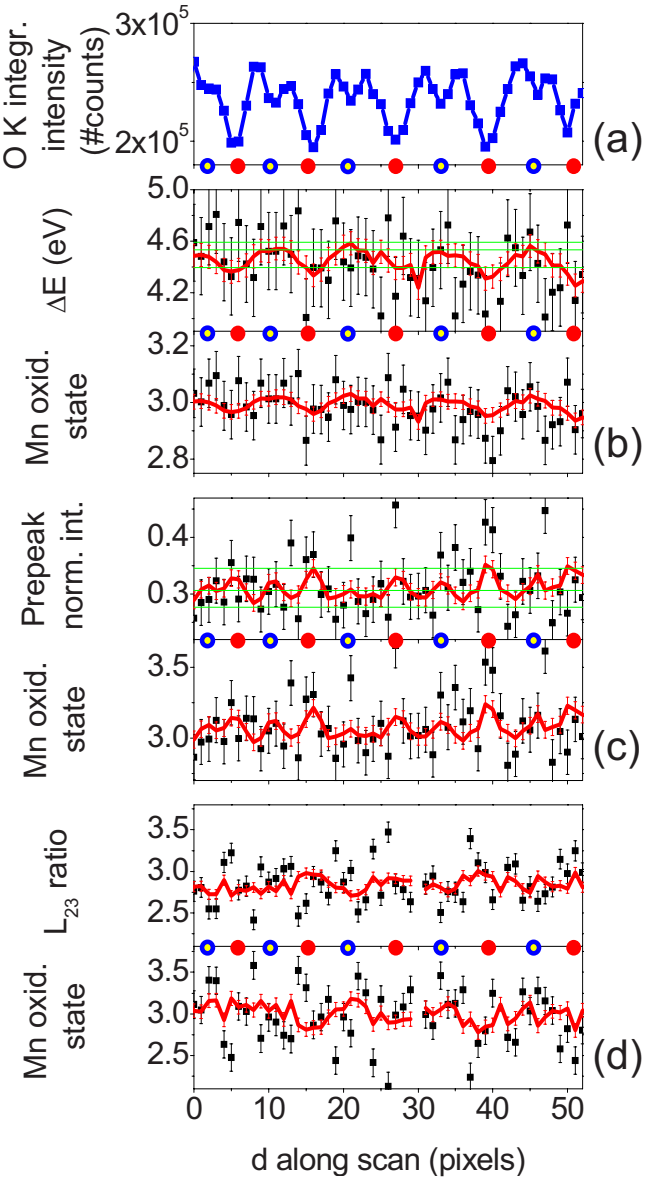

FIG. 11. (Color online) Analysis of the EELS fine structures for the LMO line scan in Fig. 7. (a) O *K* integrated intensity along the ⟨110⟩ pseudocubic diagonal [from Fig. 8(b)]. The positions of the maxima allow the Mn-O columns to be located. Blue/yellow circles show the approximate position of the Mn-O columns, while red circles show the approximate position of La along the scans [from Fig. 8(b)] through the whole figure. (b) ΔE parameter along the scan together with the derived value of the Mn oxidation state. (c) O *K* edge normalized pre-peak intensity along the line scan, together with the Mn oxidation state calculated from this measurement. (d) L_{23} ratio along the line scan and the resulting Mn oxidation state (red). A data point at $x=30$ giving rise to an unphysical Mn oxidation state value around 14 units (resulting from a spurious error during L_{23} quantification) has not been plotted. In all cases, Mn oxidation states have been derived applying the calibration shown in Figs. 1 and 2. Black squares are the result of the analysis of raw EELS data, while red lines show the result of analysis after PCA. Horizontal green lines show the values ensuing from the analysis of averaged EEL O *K* spectra, shown in Table I (the L_{23} ratio values have not been shown since they are quite flat along the scan).

sion and are more accurate, consistent with the reduced error bars on Fig. 2. It is also worth noting that any possible artifact derived from the application of PCA is less likely to affect peak positions, so the ΔE method would in principle expected to be the less influenced by PCA filtering.

The data points resulting from the analysis of raw data show significant random noise, which is not surprising since the individual spectra are noisy. However, a close inspection of the data sets obtained after PCA treatment (and the ensuing random noise removal) shows further structure in the data, which is consistent with the analysis of averaged EEL spectra summarized in Table I. This fact highlights again the relevance of such methods when looking for relevant information in noisy signals, but also that care must be taken when employing them. In what follows we will only discuss the analysis resulting from EEL spectra after PCA. It is worth noting here that, in principle, the Mn oxidation states obtained along these line scans by applying our calibrations must not be taken as actual values of this electronic property. What we attempt here is to quantify the magnitude of the Mn valence by directly applying our calibration methods in a continuous way along the electron-beam path. Later we will discuss the meaning of these changes, and the most appropriate positions where the beam must be placed in order to quantify the actual oxidation state of the Mn-O column. Interestingly, Fig. 11(b) shows a ripple with atomic periodicity [Fig. 11(d) also shows some indication, but it is too noisy to extract firm conclusions]. Figure 11(c) shows also a clear oscillatory behavior, but with double the lattice periodicity. The amplitudes of these ripples are fairly large: in some cases they convert into 0.2 valence units. This value is consistent with the analysis of averaged raw data presented in Fig. 10 and Table I, and the error bars are comparable. These changes may be sometimes close to the error bars, but the fact that we have several periods within the line scan and the behavior is periodic shows that the effects are real, and furthermore allows us to improve the statistics by averaging over several unit cells. A quick inspection of the LCMO phase diagram[1,52] reveals how such a change in the Mn valence of 0.2 or 0.3 units induced by Ca doping is very significant: large enough to transform the antiferromagnetic insulator LMO into a ferromagnetic insulator, or a ferromagnetic metal exhibiting colossal magnetoresistance, respectively. Therefore, understanding these oscillations is a key issue and deserves further attention.

In order to interpret the data in Table I and Fig. 11 it is of the utmost importance to clarify which atomic columns are being probed when the electron beam is scanned across the unit cell. As shown in Fig. 9, pure O columns (marked with a dotted square) provide approximately 25% of the total O K signal when the probe is located above the Mn-O column and 80% of the total signal when located above the La (or Ca) columns. These proportions must be kept in mind since there are nonequivalent O sites in the manganite structure. Mn is in octahedral coordination in these compounds and for LMO it also causes a Jahn-Teller (JT) distortion. We will refer to the apical O as O1, and to the JT distorted sites as O2 (marked on Fig. 12). Unfortunately, simultaneous routine acquisition of electron-diffraction patterns in the dedicated STEM is not possible, so we cannot tell *a priori* where non-

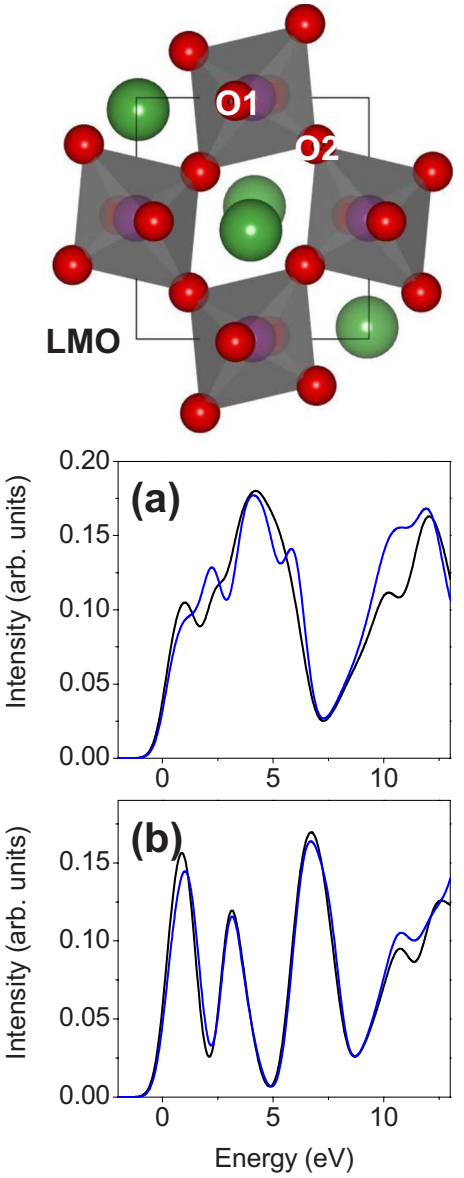

FIG. 12. (Color online) The top panel shows the LMO structure, and the positions of O1 and O2, from Ref. 54. O1 sits in the apex of the JT distorted O octahedron, while O2 is sitting at the equatorial position. The Mn-O1 bond length is 1.968 Å. The O2 is the Jahn-Teller active site and the Mn-O2 bond lengths are 1.907 Å (short) and 2.178 Å (long). The rest of the figure shows the O K edge simulations using the VASP code and the $Z+1$ approach (1 eV broadening was used) for the nonequivalent O1 and O2 sites in (a) LMO and (b) CMO. Black is used for O1 and blue for O2, for both materials. The fine structure of these edges is consistent with the experimental data in Fig. 2(a). These simulations do not include orientation effects, which could lead to further minor variations [details about the fine-structure interpretation will be discussed elsewhere (Ref. 55)].

equivalent types of O are located in our images. But $Z+1$ EELS simulations presented in Fig. 12 suggest that spectra from these nonequivalent O1 and O2 atoms should display slightly different features. Figure 12(a) shows the simulated O K edge for LMO: O1 in black and O2 in blue. Small, but noticeable changes are seen in the pre-peak position: for O2

its center of gravity is shifted (between 1 and 2 eV) toward higher energies. A minor increase in the pre-peak intensity is also observed. These changes are not surprising since LMO has a strong JT distortion and therefore O1 and O2 have a noticeably different crystal environment.

With these calculations and the O *K* simulated images (Fig. 9) in mind, we next discuss whether the nonequivalent O species can be located by EELS. For the LMO data, we should observe a larger value of ΔE in spectra obtained on columns containing a significant amount of O1 atoms, compared to those from columns with O2 atoms. The effect to be observed in actual experiments may not be as large as the ones suggested by Fig. 12(a) due to the somewhat averaging effect of dechanneling and to the long-range nature of the O *K* EELS potential as seen in Fig. 9(b), but it should be noticeable. Indeed, the experimental ΔE parameter shows a small but clear oscillation when moving from Mn-O to La columns [see Fig. 11(b)]. At first glance, the oscillation amplitude is around 0.25 eV from peak to valley, which is just above the error bars, with ΔE peaking on Mn-O columns. Since we have five periods in the scan, it is possible to improve the error bars by simple averaging. If we extract the average values of ΔE on and in between Mn-O columns we obtain values of 4.53 ± 0.02 and 4.33 ± 0.02 eV, respectively (these error bars are the standard deviation of the set, made of the five values). The difference from valley to top is 0.2 eV, which is well above 2σ, i.e., perfectly statistically significant. This ripple allows us to infer the locations of nonequivalent O atoms. According to our simulations the ripple in Fig. 11(b) is only possible if the O1 atoms in this LMO sample are located in the Mn-O column, and the four pure O column neighbors are composed of O2 atoms. Since these oscillations are indeed small, the calculated values of Mn oxidation states are relatively flat along the scan. The ensuing average Mn oxidation state calculated from ΔE on Mn-O columns is $+3.016 \pm 0.007$, while in the dips is 2.962 ± 0.007. Also, Fig. 11(b) suggests that the values obtained on top of the Mn-O columns are in better agreement with the expected nominal ones.

Theoretical simulations also allow us to understand the behavior of the normalized pre-peak intensities. The maximum amplitude (peak to valley) in Fig. 11(c) is below 0.05 normalized pre-peak intensity units, with the pre-peak intensity values being smaller on average on the center of the Mn-O columns than on La columns. This is fully consistent with (a) the analysis of raw averaged spectra, and (b) O2 first neighbors for the Mn-O column, since in the simulations in Fig. 12 the intensity of the pre-peak feature in the spectrum from O2 atoms shows a small increase. This finding is in perfect agreement with our previous interpretation of the ΔE measurement, showing that it is indeed possible to tell O1 from O2 based on the O *K* edge fine structure. Most striking, however, is an oscillation of the normalized pre-peak intensity that displays a periodicity double that of the O positions along the scan. It shows an inverted volcanolike structure that reflects the behavior of the O *K* edge intensity. This contrast may have its origin in the fact that the normalized pre-peak images are calculated through the ratio of two oscillating images. The normalized image can reflect the behavior of those used to calculate the ratio, so the volcanolike oscillation of the normalized pre-peak may be in part an artifact derived from the ratio calculation. Unfortunately, we cannot prove this conjecture beyond doubt since at present we have no codes that allow simulation of EELS fine structures combined with probe propagation dynamical effects. All we can say is that the analysis of averaged raw EEL spectra also shows a value of the pre-peak intensity which is significantly higher on the volcano dip than on the rim, so this oscillation is not an artifact of PCA. Regardless, the Mn valence derived in between Mn-O columns shows the biggest departure from the nominal expected values. Therefore, we suggest that when using the pre-peak intensity to obtain oxidation states with atomic size electron probes the most dependable values will be obtained when the beam is located slightly off the column, on the volcano rim (if present).

For measurements using the L_{23} ratio, a slight dependence on the relative position of the electron beam and the Mn-O column is occasionally observed (as we will discuss later), although it is not clear in Fig. 11(d). When observed, the oscillations also reflect the ripple in the total Mn signal. In these cases, the L_{23} ratio is also a ratio between signals with an atomic oscillation in them (both the L_3 and the L_2 line intensities oscillate with atomic periodicity). Therefore it may again be an artifact derived from the normalization process. Unfortunately, the normalization could not be avoided in any of these methods since un-normalized integrated peak intensities do not represent a direct source of DOS related information. The whole edge intensity in bulk, average, on-axis measurements directly depends on the probe position (on/off column) in atomic resolution images. Normalization is necessary to remove thickness or concentration effects, although it may not completely get rid of the atomic contrast ripple. The analysis of the principal components resulting from PCA may be a way to extract site-dependent information on electronic properties or the unoccupied DOS. However, the interpretation of the meaning of individual components and their connection to actual features related to the physical properties is not necessarily straightforward. Again, we suggest that Mn oxidation state values derived from L_{23} ratios seem to generate values closer to the expected nominal ones when the electron probe is located on the Mn-O column. However, without codes that include both fine-structure effects and probe scattering, we cannot fully explain these effects. Fortunately, the maximum variations in oxidation states are of the order, or below, 10% from the highest maxima to the valleys, so these possible artifacts do not completely impede imaging of oxidation states with atomic resolution. In summary, it seems that the ΔE method is the more accurate and reliable method for Mn valence determination.

Materials that do not exhibit strong JT distortions, such as CMO, do not exhibit such noticeable changes between nonequivalent O species. Figure 12(b) shows the simulated O *K* spectra for CMO. No major differences are observed between O1 and O2, other than a very small decrease in pre-peak intensity. Accordingly, the ΔE images for CMO are relatively flat: the difference in ΔE for O1 and O2 is minimal, and dechanneling effects together with the broad O *K* potential would tend to smear these, already small, differences. An example is shown in Fig. 6(b), where, unsurprisingly, the atomic lattice is not resolved. However, the O

atomic lattice is clearly observed in the pre-peak image in Fig. 6(c). The pre-peak intensity exhibits the lattice modulation, with maxima on the Mn-O columns and minima in between (although the volcano geometry in not transferred to the pre-peak image in this case). If we interpret these dips in terms of nonequivalent O positions by looking at the simulations in Figs. 9(c) and 12(b), we conclude that the Mn-O columns in this sample are mainly composed of apical O1 atoms while the pure O columns are mainly O2.

X. SUMMARY

In summary, we have compared three different methods to obtain the average oxidation state of Mn in manganite oxides by analyzing the O *K* edge and the Mn $L_{2,3}$ edge fine structures. All three methods show results that are consistent with each other, and linear relationships between measurable magnitudes such as the O *K* normalized pre-peak intensity, the O *K* ΔE parameter (main peak to pre-peak separation) or L_{23} ratios with Mn oxidation state have been obtained from the analysis of average EEL spectra. Although the ΔE method is the most accurate and dependable one for bulk samples, all three relationships can be used as external calibrations to obtain Mn oxidation states in manganites (as long as similar detector geometries are used), so we have applied them to atomic resolution images. It is worth noting here that oxidation states measured from EELS are not related to real charge states around given atoms. EELS measurements are only sensitive to the DOS (i.e., electronic properties such as the 3*d* band occupancy), but not to total charge densities.[38]

When these methods are applied to EELS data acquired with atomic size electron probes, electron energy-loss near-edge structure spatial variations related to the atomic structure are observed. Mn valence can still be quantified, although it shows unexpected oscillations linked to the underlying Mn lattice. In these cases, it seems that the L_{23} ratios show better results when the electron beam is on the Mn-O column. We do not fully understand the reason yet but, fortunately, such effects are small and in most cases close to the error bars of the experiment itself. On the other hand, the ΔE method seems to be the most accurate, and we have shown that it is capable of extracting additional information on the DOS with atomic resolution, specifically, it is able to discriminate between nonequivalent O species in LMO. Similar information is available from the O *K* pre-peak normalized intensity method, although it is less accurate. 2D images of CMO were acquired, showing for the first time 2D images of the volcano dip in O *K* images. These 2D images are too noisy to extract reliable information on nonequivalent O species. Nevertheless, upon improvements of the optics and acquisition conditions in the STEM, we envision this method as a most promising one toward future two-dimensional mapping of 3*d* orbital related information in this class of materials.

ACKNOWLEDGMENTS

The authors are grateful to W. Tian and D. Mandrus for providing the LMO and CMO powders, to J. Santamaria for the $La_{0.7}Ca_{0.3}MnO_3$ film and to D. Niebieskikwiat and M. B. Salamon for the polycrystalline $La_{0.55}Ca_{0.45}MnO_3$ sample. Fruitful discussions with R. Sanchez are also acknowledged (M.V.). Research at ORNL (M.V., S.J.P.) was sponsored by the Office of Basic Energy Sciences, Division of Materials Sciences and Engineering of the U.S. Department of Energy and by an appointment to the ORNL Postdoctoral Research Program administered jointly by ORNL and ORISE (J.T.). Research at Vanderbilt University was sponsored by the DOE Office of Basic Energy Sciences, Division of Materials Sciences and Engineering (W.L., M.P.O.) and by the McMinn Endowment at Vanderbilt University (S.T.P.). Computations were performed at the National Energy Research Scientific Computing Center.

*Present address: Condensed Matter Physics & Materials Science Department, Brookhaven National Laboratory, Upton, New York 11973, USA.

†Present address: Lehigh University, Bethlehem, PA 18025, USA.

[1] E. Dagotto, T. Hotta, A. Moreo. Phys. Rep. **344**, 1 (2001).

[2] N. D. Browning, M. F. Chisholm, and S. J. Pennycook, Nature (London) **366**, 143 (1993).

[3] M. Varela, S. D. Findlay, A. R. Lupini, H. M. Christen, A. Y. Borisevich, N. Dellby, O. L. Krivanek, P. D. Nellist, M. P. Oxley, L. J. Allen, and S. J. Pennycook, Phys. Rev. Lett. **92**, 095502 (2004).

[4] M. Bosman, V. J. Keast, J. L. Garcia-Muñoz, A. J. D'Alfonso, S. D. Findlay, and L. J. Allen, Phys. Rev. Lett. **99**, 086102 (2007).

[5] K. Kimoto, T. Asaka, T. Nagai, M. Saito, Y. Matsui, and K. Ishizuka, Nature (London) **450**, 702 (2007).

[6] P. D. Nellist and S. J. Pennycook, Phys. Rev. Lett. **81**, 4156 (1998).

[7] P. D. Nellist, M. F. Chisholm, N. Dellby, O. L. Krivanek, M. F. Murfitt, Z. S. Szilagyi, A. R. Lupini, A. Y. Borisevich, W. H. Sides, and S. J. Pennycook, Science **305**, 1741 (2004).

[8] M. Varela, A. R. Lupini, K. van Benthem, A. Y. Borisevich, M. F. Chisholm, N. Shibata, E. Abe, and S. J. Pennycook, Annu. Rev. Mater. Res. **35**, 539 (2005).

[9] D. A. Muller, L. Fitting-Kourkoutis, M. Murfitt, J. H. Song, H. Y. Wang, J. Silcox, N. Dellby, and O. L. Krivanek, Science **319**, 1073 (2008).

[10] R. F. Egerton, *Electron Energy Loss in the Electron Microscope*, 2nd ed. (Plenum, New York, 1996).

[11] J. H. Rask, B. A. Miner, and P. R. Buseck, Ultramicroscopy **21**, 321 (1987).

[12] O. L. Krivanek and J. H. Paterson, Ultramicroscopy **32**, 313 (1990).

[13] J. H. Paterson and O. L. Krivanek, Ultramicroscopy **32**, 319 (1990).

[14] H. Kurata and C. Colliex, Phys. Rev. B **48**, 2102 (1993).

[15] R. Buczko, G. Duscher, S. J. Pennycook, and S. T. Pantelides,

Phys. Rev. Lett. **85**, 2168 (2000).
[16] M. P. Oxley and L. J. Allen, Phys. Rev. B **57**, 3273 (1998).
[17] L. J. Allen, S. D. Findlay, M. P. Oxley, and C. J. Rossouw, Ultramicroscopy **96**, 47 (2003).
[18] S. D. Findlay, M. P. Oxley, S. J. Pennycook, and L. J. Allen, Ultramicroscopy **104**, 126 (2005).
[19] R. D. Leapman and L. A. Grunes, Phys. Rev. Lett. **45**, 397 (1980).
[20] P. A. Van Aken and B. Liebscher, Phys. Chem. Miner. **29**, 188 (2002).
[21] T. Sparrow, B. Williams, C. Rao, and J. Thomas, Chem. Phys. Lett. **108**, 547 (1984).
[22] T. Riedl, T. Gemming, W. Gruner, J. Acker, and K. Wetzig, Micron **38**, 224 (2007).
[23] C. Mitterbauer, G. Kothleitner, W. Grogger, H. Zandbergen, B. Freitag, P. Tiemeijer, and F. Hofer, Ultramicroscopy **96**, 469 (2003).
[24] A. L. Ankudinov, A. I. Nesvizhskii, and J. J. Rehr, Phys. Rev. B **67**, 115120 (2003).
[25] S. P. Cramer, F. M. F. de Groot, Y. Ma, C. T. Chen, F. Sette, C. A. Kipke, D. M. Eichhorn, M. K. Chan, W. H. Armstrong, E. Libby, G. Christou, S. Brooker, V. McKee, O. C. Mullins, and J. C. Fuggle, J. Am. Chem. Soc. **113**, 7937 (1991).
[26] F. M. F. de Groot, J. Electron Spectrosc. Relat. Phenom. **67**, 529 (1994).
[27] F. de Groot, Coord. Chem. Rev. **249**, 31 (2005).
[28] W. G. Waddington, P. Rez, I. P. Grant, and C. J. Humphreys, Phys. Rev. B **34**, 1467 (1986).
[29] D. H. Pearson, B. Fultz, and C. C. Ahn, Appl. Phys. Lett. **53**, 1405 (1988).
[30] D. H. Pearson, C. C. Ahn, and B. Fultz, Phys. Rev. B **47**, 8471 (1993).
[31] Z. L. Wang, J. S. Yin, and Y. D. Jiang, Micron **31**, 571 (2000).
[32] R. D. Leapman, P. Rez, and D. F. Meyers, J. Chem. Phys. **72**, 1232 (1980).
[33] C. C. Ahn and P. Rez, Ultramicroscopy **17**, 105 (1985).
[34] R. D. Leapman, L. A. Grunes, and P. L. Fejes, Phys. Rev. B **26**, 614 (1982).
[35] B. T. Thole and G. van der Laan, Phys. Rev. B **38**, 3158 (1988).
[36] L. A. Grunes, R. D. Leapman, C. N. Wilker, R. Hoffmann, and A. B. Kunz, Phys. Rev. B **25**, 7157 (1982).
[37] F. M. F. de Groot, M. Grioni, J. C. Fuggle, J. Ghijsen, G. A. Sawatzky, and H. Petersen, Phys. Rev. B **40**, 5715 (1989).
[38] W. Luo, A. Franceschetti, M. Varela, J. Tao, S. J. Pennycook, and S. T. Pantelides, Phys. Rev. Lett. **99**, 036402 (2007).
[39] C. Jeanguillaume and C. Colliex, Ultramicroscopy **28**, 252 (1989).
[40] J. A. Hunt and D. B. Williams, Ultramicroscopy **38**, 47 (1991).
[41] M. P. Oxley, M. Varela, T. J. Pennycook, K. van Benthem, S. D. Findlay, A. J. D'Alfonso, L. J. Allen, and S. J. Pennycook, Phys. Rev. B **76**, 064303 (2007).
[42] M. P. Oxley, E. C. Cosgriff, and L. J. Allen, Phys. Rev. Lett. **94**, 203906 (2005).
[43] A. J. D'Alfonso, S. D. Findlay, M. P. Oxley, and L. J. Allen, Ultramicroscopy **108**, 677 (2008).
[44] E. L. Shirley, Phys. Rev. Lett. **80**, 794 (1998).
[45] L. X. Benedict, E. L. Shirley, and R. B. Bohn, Phys. Rev. Lett. **80**, 4514 (1998).
[46] M. Rohlfing and S. G. Louie, Phys. Rev. Lett. **81**, 2312 (1998).
[47] R. R. Meyer and A. Kirkland, Ultramicroscopy **75**, 23 (1998).
[48] R. R. Meyer and A. Kirkland, Microsc. Res. Tech. **49**, 269 (2000).
[49] M. Bosman, M. Watanabe, D. T. L. Alexander, and V. J. Keast, Ultramicroscopy **106**, 1024 (2006).
[50] R. F. Egerton and S. F. Cheng, Ultramicroscopy **21**, 231 (1987).
[51] J. M. LeBeau, S. D. Findlay, L. J. Allen, and S. Stemmer, Phys. Rev. Lett. **100**, 206101 (2008).
[52] S.-W. Cheong and H. Y. Hwang, in *Contribution to Colossal Magnetoresistance Oxides, Monographs in Condensed Matter Science*, edited by Y. Tokura (Gordon and Breach, London, 1999).
[53] Y. Ito, R. F. Klie, N. D. Browning, and T. J. Mazanec, J. Am. Ceram. Soc. **85**, 969 (2002).
[54] J. Rodriguez-Carvajal, M. Hennion, F. Moussa, A. H. Moudden, L. Pinsard, and A. Revcolevschi, Phys. Rev. B **57**, R3189 (1998).
[55] W. Luo, M. Varela, J. Tao, S. J. Pennycook, and S. T. Pantelides Phys. Rev. B **79**, 052405 (2009).